ACS NANO

www.acsnano.org

ARTICLE

Super-resolved Optical Mapping of Reactive Sulfur-Vacancies in Two-Dimensional Transition Metal Dichalcogenides

Miao Zhang,* Martina Lihter, Tzu-Heng Chen, Michal Macha, Archith Rayabharam, Karla Banjac, Yanfei Zhao, Zhenyu Wang, Jing Zhang, Jean Comtet, Narayana R. Aluru, Magalí Lingenfelder, Andras Kis, and Aleksandra Radenovic*

Cite This: *ACS Nano* 2021, 15, 7168–7178

Read Online

ACCESS | Metrics & More | Article Recommendations | Supporting Information

ABSTRACT: **Transition metal dichalcogenides (TMDs) represent a class of semiconducting two-dimensional (2D) materials with exciting properties. In particular, defects in 2D-TMDs and their molecular interactions with the environment can crucially affect their physical and chemical properties. However, mapping the spatial distribution and chemical reactivity of defects in liquid remains a challenge. Here, we demonstrate large area mapping of reactive sulfur-deficient defects in 2D-TMDs in aqueous solutions by coupling single-molecule localization microscopy with fluorescence labeling using thiol chemistry. Our method, reminiscent of PAINT strategies, relies on the specific binding of fluorescent probes hosting a thiol group to sulfur vacancies, allowing localization of the defects with an uncertainty down to 15 nm. Tuning the distance between the fluorophore and the docking thiol site allows us to control Föster resonance energy transfer (FRET) process and reveal grain boundaries and line defects due to the local irregular lattice structure. We further characterize the binding kinetics over a large range of pH conditions, evidencing the reversible adsorption of the thiol probes to the defects with a subsequent transitioning to irreversible binding in basic conditions. Our methodology provides a simple and fast alternative for large-scale mapping of nonradiative defects in 2D materials and can be used for *in situ* and spatially resolved monitoring of the interaction between chemical agents and defects in 2D materials that has general implications for defect engineering in aqueous condition.**

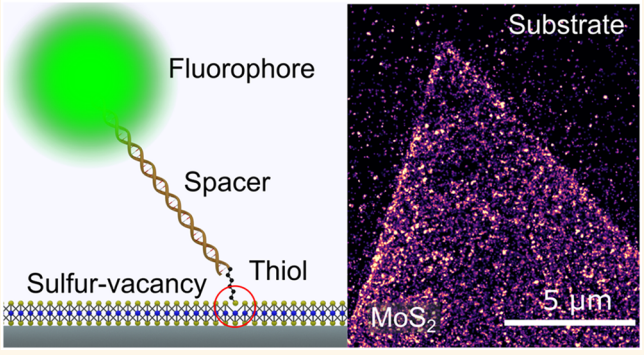

KEYWORDS: *2D materials, defects, super-resolution, thiol chemistry, sulfur vacancy, interface*

The emerging class of two-dimensional (2D) materials, such as graphene, hexagonal boron nitride (h-BN), and transition metal dichalcogenide (TMD) monolayers, shows exciting physical properties that are distinct from their bulk forms. Even more fascinating is the ubiquity of defects in 2D materials, which can profoundly alter the properties of materials and interact strongly with the external environment. Defects are often detrimental for the performance of semiconductor devices based on 2D materials in terms of low carrier mobility and low photoluminescence (PL)[1,2] but can be in turn exploited as single-photon emitters,[3,4] to introduce magnetism,[5] to fabricate memristive devices,[6,7] or as catalysts[8,9] and recently as probes to sense single-proton hopping in aqueous solvent.[10] Although defects in 2D materials have been extensively studied in vacuum or air at atomic resolution by transmission electron microscopy and scanning tunneling microscopy[11−14] and at large-scale by optical microscopy and spectroscopy,[3,15,16] large-scale mapping of defects and characterization of their reactivity at liquid interfaces is yet to be explored. In particular, the lack of fundamental understanding of defects at solid/liquid interface hinders further development in 2D material-based nanofluidics,[17,18] osmotic power generation,[19,20] catalysis,[20,21] and so forth. There is thus a clear need for a simple and inexpensive method that could quickly characterize a large area of defects

Received: January 14, 2021
Accepted: April 2, 2021
Published: April 8, 2021

https://doi.org/10.1021/acsnano.1c00373
ACS Nano 2021, 15, 7168–7178

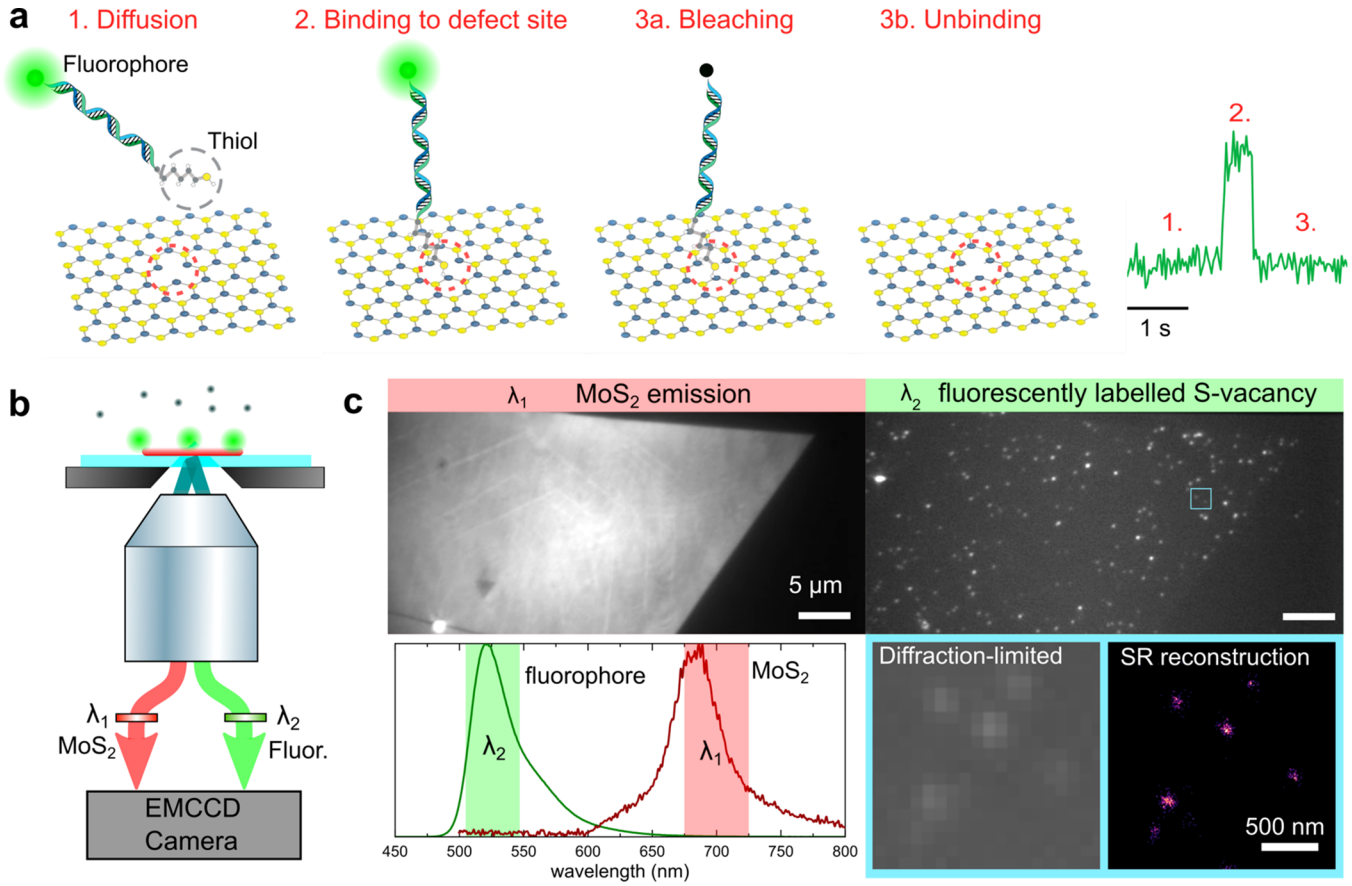

Figure 1. Working principle of thiol-chemistry-assisted super-resolution optical mapping of sulfur vacancies in 2D transition metal dichalcogenides. (a) Fluorophores with emission wavelength clearly distinguishable from the photoluminescence (PL) of MoS_2 are conjugated with dsDNA linker molecules and docking thiol molecules (1). The selective adsorption of thiol molecules at sulfur vacancies allows the labeling of these defects (2). The bleaching of fluorophores (3a) and the dynamics of the adsorption/desorption of thiol molecules (3b) yields an intermittent fluorescent signal from the fluorophores bound to a defect site, which allows the application of single-molecule localization microscopy. (b) The optical setup is based on total internal reflection fluorescent microscopy. The evanescent wave of the laser beam confines excitation and photoluminescence (PL) emissions from MoS_2 and fluorophores to ~100 nm from the surface, collected by a 100 × NA 1.49 oil immersion objective lens. The emission signals from MoS_2 and the fluorophores are then split into two paths according to their wavelength and projected side-by-side on an EMCCD camera (see Figure S1 for setup) (c) PL images of a MoS_2 flake (path λ_1) and fluorescently labeled sulfur vacancies (path λ_2) are collected simultaneously. The images were taken with ATTO-dsDNA70bp-SH probes with a concentration of 100 pM under excitation power of ~5 W/cm^2. Images shown here are averaged over 1000 frames for clarity. The bottom panel shows the spectra of ATTO488 fluorophores and a monolayer MoS_2. The spectrum ranges of the bandpass filters are marked in green and red. PL image (standard deviation of 10^4 frames) of the zoomed-in area highlighted in the blue-square showing diffraction-limited fluorescent pattern due to individual thiol molecules. After localization of the position of each molecule, the overlay of the centroid positions of the detected molecules in each frame yields the reconstructed super-resolution (SR) map.

in 2D materials that would operate across different environments (air, liquid, liquid confinement) in order to investigate the wealth of dynamic phenomena at solid−liquid interfaces.

To address these questions, we recently demonstrated wide-field mapping of proton-activated photon-emitting defects in hBN in liquid with a spatial resolution down to 10 nm by one of the super-resolution microscopy techniques, called single molecule localization microscopy (SMLM).[22,23] The subdiffractional resolution is achieved by locating the sparse single emitters by fitting the point-spread functions. The precision of the localization increases with the square root of the number of the detected photons as $\sqrt{N}$.[24] However, for the most abundant point defects in TMDs, for example the sulfur vacancies in MoS_2 and WS_2, SMLM cannot be directly applied due to their nonradiative nature at room temperature.[11,16,25]

Here, we demonstrate large-area visualization of the spatial distribution of nonradiative defects in 2D materials in aqueous solutions, using thiol-functionalized fluorescent probes that specifically interact with reactive sulfur vacancies.[26−30] In this scenario, the fluorescent probes transiently bind to the sulfur vacancies, which leads to blinking signals from the labeled defects that allow us to apply single molecule localization. Our method, reminiscent of PAINT (point accumulation for imaging in nanoscale topography) strategies that are previously used to study biological samples and synthetic materials,[31−35] is abbreviated as 2D-PAINT hereafter. By direct observation, we establish the binding affinity and specificity of the thiol-functionalized probes to the sulfur vacancies and reveal a correlation between the defect density and the PL emission of the TMD monolayers. By varying the distance between the fluorophore and the docking thiol group, we can further control Föster resonance energy transfer (FRET) induced fluorescent quenching[36,37] and reveal fine details of grain boundaries and line defects. In addition, we systematically

https://doi.org/10.1021/acsnano.1c00373
ACS Nano 2021, 15, 7168−7178

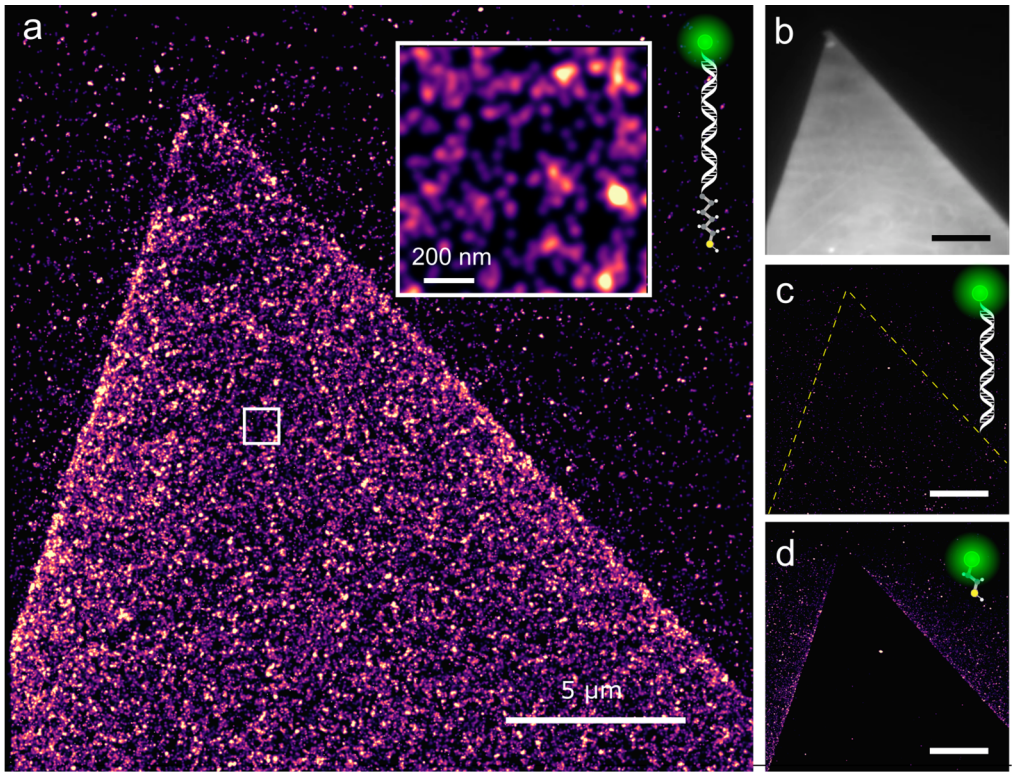

Figure 2. The affinity of thiol binding on MoS_2 surface: 2D-PAINT reconstructed images of a MoS_2 flake with fluorescent probes of different compositions. (a) The 2D-PAINT image acquired using fluorescent probes consisting of a fluorophore head, dsDNA of 70bp as linker molecule, and a thiol tail (FAM-dsDNA70bp-SH). The zoomed-in image reveals a high density of binding on MoS_2. (b) An averaged PL image of the MoS_2 flake in (a) with a perfect 60° triangle shape and homogeneous PL intensity. (c) The 2D-PAINT image acquired using fluorescent probes without thiol groups (FAM-dsDNA70bp). (d) The 2D-PAINT image acquired using fluorophores that directly conjugated with thiol (ATTO-SH). All experiments are performed with 40 nM concentration of the probes. The 2D-PAINT images are reconstructed from 10^4 frames with normalized Gaussian rendering. Scale bars in (a−d) are 5 μm.

study the binding kinetics between thiols and sulfur vacancies and find out that the reversible interaction under illumination can be turned into irreversible binding by the pH-dependent deprotonation of thiol. Our work demonstrates a general method for mapping of a broad range of nonradiative defects in 2D materials in liquid and can be used for *in situ* and spatially resolved monitoring of the interaction between chemical agents and defects in 2D materials that can potentially lead to defect healing, 2D material modification, as well as biosensing applications.

RESULTS AND DISCUSSION

Principles of 2D-PAINT and Experimental Conditions.

The principle of 2D-PAINT is to map the spatial distribution of defects by detecting the transient fluorescence signals coming from the interaction of a specifically functionalized fluorophore with the targeted defect, as depicted in Figure 1a. To enable detectable transient labeling of sulfur vacancies, we design probes as a double-stranded (ds) DNA in which each end is modified with a fluorophore and C6-thiol, respectively. Varying the DNA length allows us to control FRET-induced fluorescent quenching. A total internal reflection fluorescence (TIRF) microscope is used to image labeled sulfur vacancies in MOCVD-grown monolayer of MoS_2 flakes with a minimized PL background from the free diffusing probes in solution. Prior to imaging, MoS_2 flakes are transferred to glass coverslips.[38] The fluorophores ATTO488 and fluorescein amidite (FAM) with an emission peak at 520 nm are selected to avoid overlapping with PL emission of MoS_2, which is typically between 590−720 nm (i.e., 1.7−2.2 eV)[39,40] (Figure 1c). A laser with a wavelength of 488 nm excites both the fluorophores and the MoS_2 through an oil immersion TIRF objective lens. The PL image is split into two paths corresponding to the fluorophore and MoS_2 emission, respectively, as shown in Figure 1b,c. This simultaneous imaging allows us to correlate the defect distribution and the photoluminescence of the 2D-TMDs. A high concentration salt buffer (400 mM KCl 40 mM Tris buffer pH ∼ 7.7) is used to shield the electrostatic repulsion between the negatively charged MoS_2 surface and the negatively charged DNA molecules. In the absence of the oxygen-scavenger in buffer, fluorescent probes that attach to the surface bleach rather quickly under the continuous excitation of the 488 nm laser, such that only a fraction of the attached probes is detectable on each frame allowing for localization. As can be seen in the zoomed-in images in Figure 1c, PL signal from a single fluorescent thiol label spreads over ∼5-by-5 pixels (pixel size = 105 nm) according to the point spread function of the optical system. The centroids of the molecules imaged in each frame are localized by 2D-Gaussian fitting with the localization precision that scales inversely with square root of total number of emitted photons.[24] We obtain the best precision of ∼15 nm with ATTO488 fluorophore under excitation power of 67 W/cm^2. Detailed description of the localization procedure can be found in Methods.

https://doi.org/10.1021/acsnano.1c00373
ACS Nano 2021, 15, 7168−7178

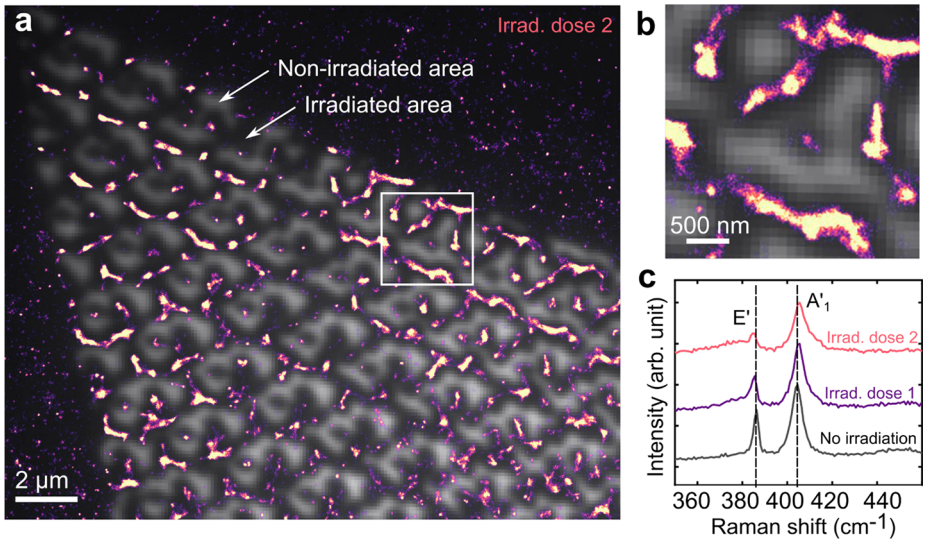

Figure 3. Specific binding of thiol probe on sulfur vacancy defects: 2D-PAINT imaging on FIB prepatterned MoS_2. (a) Overlay of a PL image (gray scale) and a 2D-PAINT reconstructed image (color-coded) taken on a prepatterned MoS_2 flake by the focused-ion beam at dose of 1.1×10^{14} ions/cm^2. The 2D-PAINT image is reconstructed from 5×10^3 frames with averaged shifted histogram rendering. Imaging was performed with ATTO-dsDNA70bp-SH probes with a concentration of 10 nM under excitation power of ~19 W/cm^2. (b) Zoomed-in image of the highlighted area in (a). (c) Raman scattering spectra of MoS_2 flakes with no irradiation, irradiation dose 1 of 3.4×10^{13} ions/cm^2, and dose 2 of 1.1×10^{14} ions/cm^2.

Binding Affinity and Specificity. First, we perform 2D-PAINT imaging on MoS_2 flakes using fluorescent probes consisting of FAM dye, dsDNA of 70 base pairs and a thiol-functional group, namely FAM-dsDNA70bp-SH. The schematics of the probe with the resulting PAINT image is depicted in Figure 2a. The localizations based on the detected fluorescence of individual emitters are summed up from 10^4 frames. Brighter spots represent a higher localization density. As shown in Figure 2a with FAM-dsDNA70bp-SH probes, bindings are homogeneous over the sample with a slightly higher density of events along the edges, as shown in Figure 2a. Quantitatively, spatial autocorrelation analysis of the central area of MoS_2 yields a Moran's I value as 0.13, demonstrating a random distribution of the binding events and high homogeneity (details in SI Section 12). This binding homogeneity is consistent with the homogeneous defect distribution expected from TEM and PL measurements on a perfect triangle shape flake with homogeneous PL (see Figure 2b). Straight edges were shown previously to be Mo-terminated[41] and are thus more likely to be bound by thiol probes.

As a control experiment, we employ probes without thiol, namely FAM-dsDNA70bp. All other conditions are kept identical. As shown in Figure 2c, in contrast to the high localization density with thiol probes only a few fluorescent events are detected when the probe is switched to FAM-dsDNA70bp. Such a marked difference proves that −SH is the active group responsible for the interaction between the probes and the MoS_2 surface that yields the PL signal. AFM scanning of as-grown MoS_2 on sapphire in a buffer solution with the presence of thiol probes shows that the molecules can also physisorb with their main molecular axis parallel to the surface (Figure S11). However, such adsorption geometries not interacting directly at the defects will not contribute to the fluorescence signal due to the quenching by MoS_2 at close proximity.[36,37] Indeed, using fluorophores that are directly conjugated to ethanethiol molecules (ATTO-SH), we observe almost no fluorescence on the MoS_2 flake due to FRET, as shown in Figure 2d. These results demonstrate the necessity of the thiol functional group and the linker molecule (such as dsDNA) to enable fluorescence detection of the probe-defect interaction.

To validate the binding specificity on defects, we perform 2D-PAINT imaging on MoS_2 samples with prepatterned defective sites. A high density of defects was deliberately introduced in MoS_2 flakes by xenon focused-ion beam (FIB) irradiation.[42] Periodical patterns with a pitch distance of 2 μm are irradiated on MoS_2 with carefully tuned ion dose and dwell time to avoid complete removal of the material, which is confirmed by the Raman scattering spectra, as shown in Figure 3c and AFM (Figure S2). On irradiated samples, we observe a downshift of E′ mode and an upshift of A'_1 mode with a clearly decreasing amplitude ratio of E'/A'_1 and broadening of both peaks. In addition, disorder-induced modes emerge as the dose of irradiation increases, one of which is at the low-frequency shoulder of E′ (~377 cm^{-1}) and the other LA(M) mode at ~227 cm^{-1} (Figure S3).[43] These transitions in Raman scattering spectra strongly indicate an increasing concentration of sulfur vacancies, which has been reported previously upon ion and electron beam irradiation.[15,43,44] The highly defective crystal structures induced by the ion bombardment lead to a diminished PL emission of MoS_2, as shown in Figure 3a (gray scale). Similar PL quenching has been reported on MoS_2 with distorted lattice after oxygen plasma exposure.[44] Performing 2D-PAINT imaging on the flake using ATTO-dsDNA70bp-SH probes, we observe a highly selective binding on the irradiated area. Overlaying the reconstructed localization density map (color-coded) with the PL image of the same area demonstrates a strong correlation between the area of diminished PL and the area of high-localization density. Details of the overlay can be seen in the zoomed-in image in Figure 3b. The absence of binding in the nonirradiated area is most likely due to redeposition of the knocked-off materials that block the binding sites. The correlation between the

https://doi.org/10.1021/acsnano.1c00373
ACS Nano 2021, 15, 7168−7178

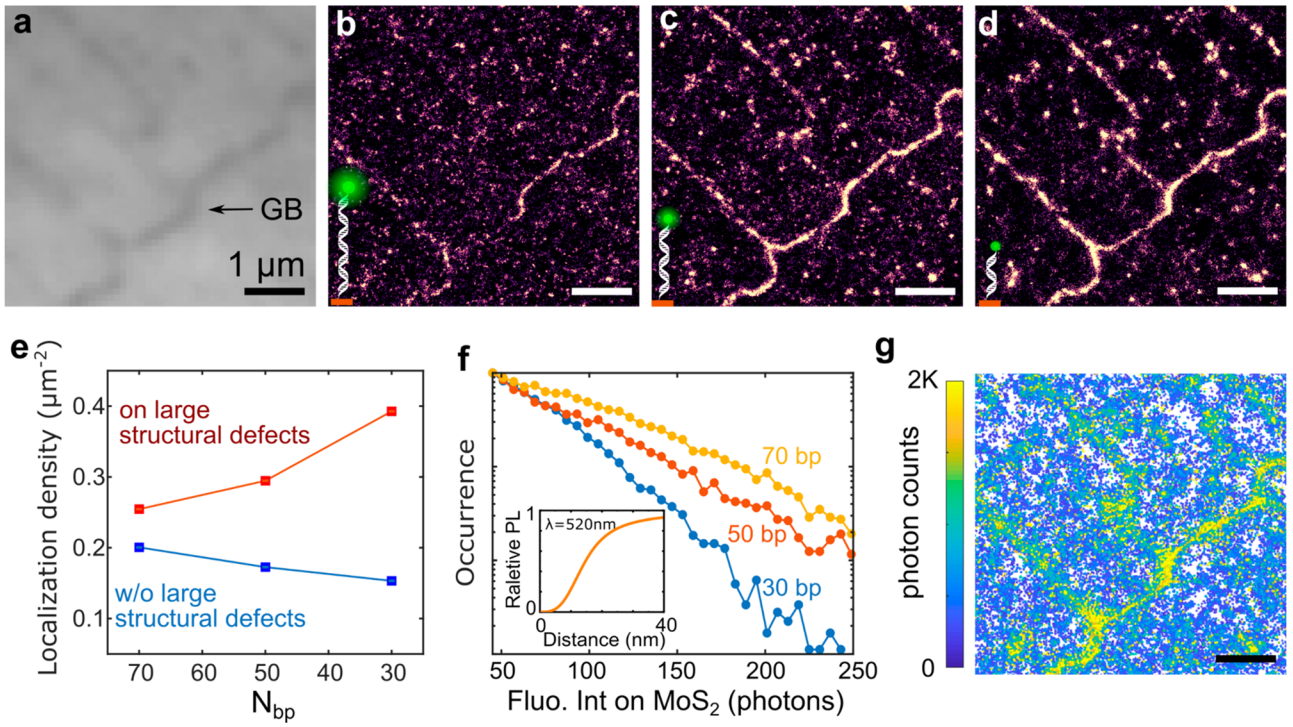

Figure 4. Fluorescent probes with varied DNA linker lengths reveal large structural defects on MoS_2 (a) An image of PL emission of monolayer-MoS_2 consisting of large structural defects, including a grain boundary (GB) and line defects. (b–d) The 2D-PAINT images taken on the same area of MoS_2 flake using fluorescent thiol probes ATTO-dsDNA-SH with dsDNA length of 70bp, 50bp, and 30bp, respectively, at 40 nM. The excitation power density is 19 W/cm^2. The images are reconstructed from 5 × 10^3 frames using averaged shifted histogram. (e) Detected localization density per frame as a function of the number of base pairs in DNA linkers. Data are extracted respectively on areas with (red) and without (blue) large structural defects. (f) Intensity histogram of ATTO-dsDNA-SH with dsDNA length of 70bp, 50bp, and 30bp on a MoS_2 flake without large structural defects. The inset shows theoretically calculated normalized intensity of the fluorophore ATTO488 emission as a function of the fluorophore distance from the MoS_2 surface. Details of the calculation can be found in Supporting Information. (g) Fluorescence intensity map of (d). Scale bars are 1 μm.

localization density and the defect density is also confirmed by performing 2D-PAINT imaging on monolayer MOCVD-grown WS_2 flakes. MOCVD-grown WS_2 is known for its inhomogeneity in PL emission due to the defect density variation across a flake.[16,45,46] The 2D-PAINT imaging reveals a strong correlation between the localization density of the fluorescent events and the PL intensity of the WS_2 flake (Figure S4). These results clearly demonstrate favorable binding between the thiol probes and the sulfur vacancies.

Nonhomogeneous FRET Reveals Large Structural Defects. The quenching effect evidenced in Figure 2d shows the necessity of the linker molecule for the imaging of defects, but tuning the linker length can also allow us to reveal grain boundaries and line defects in the 2D-crystal. We investigate the homogeneity of the FRET effect on a MoS_2 monolayer that contain grain boundaries and line defects as shown in Figure 4a. Grain boundaries and line defects that appear dark in the PL image have been reported as sulfur-deficient defects.[41] We refer to such defects as large structural defects hereafter. Figure 4b–d shows the 2D-PAINT images reconstructed from data taken with probes of 70bp, 50bp, and 30bp dsDNA, respectively, corresponding to the contour length of 24, 17, and 10 nm. The grain boundaries and line defects become clearly visible with the decreasing probe length. This even applies to the thiol probes without dsDNA linker molecules (Figure S5). Fine details of these large structural defects are revealed beyond the diffraction-limitation in the PL image. We attribute this nonhomogenous localization density to distinct FRET quenching processes in areas with and without large structural defects.

To analyze in more detail this mechanism of FRET quenching, we extracted the average localization density per frame on areas with and without large structural defects. As can be seen in Figure 4e, the localization densities on the large structural defects are higher than on the areas without the large structural defects and follow opposite trends with respect to probe length. These opposite trends in localization density are responsible for the improving contrast of the grain boundaries and the line defects in Figure 4d. The increasing binding rate on the large structural defects is consistent with an increase in the diffusion coefficient of the probe in the absence of any FRET quenching effect. The diffusion coefficient of short dsDNA scales with its number of basepairs (in other words, the contour length) as $D \propto N_{bp}^{-0.67}$.[47] The 30bp probes diffuse almost two-fold faster than the 70bp probes therefore having a higher binding rate. A similar trend is observed on the glass substrate (not shown), which is consistent with the negligible FRET processes in these areas. That this trend is opposite on areas without large structural defects can be understood based on nonradiative FRET process that reduces the PL intensity of probes, resulting in a cutoff for the low-intensity events in detection. Such truncation is more pronounced for shorter probes. As can be seen in Figure 4f, the fluorophore intensity measured on MoS_2 flakes without large structural defects increases with the increasing length of dsDNA linker molecule. The theoretical calculation shows that the effective range of

https://doi.org/10.1021/acsnano.1c00373
ACS Nano 2021, 15, 7168–7178

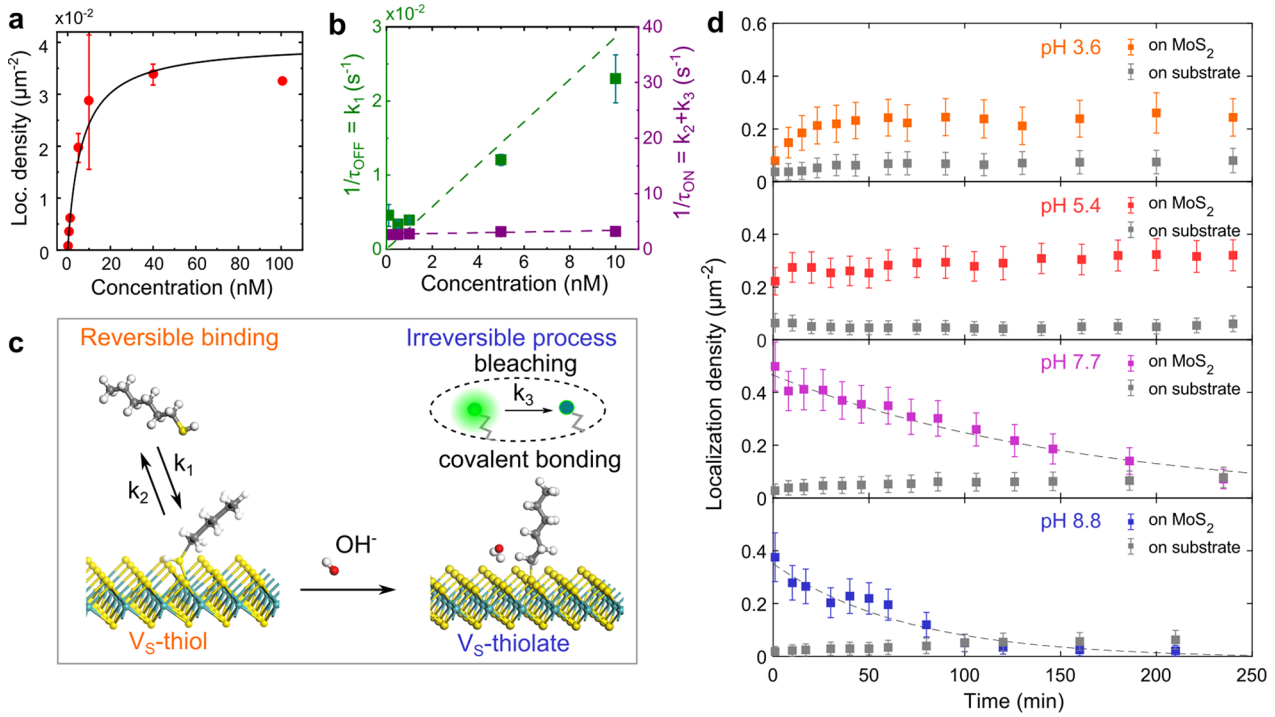

Figure 5. pH-dependent binding kinetics between thiol and sulfur vacancies. (a) Langmuir adsorption isotherm of FAM-dsDNA70bp-SH binding to a MoS_2 monolayer in reversible binding regime at pH 7.7 with the black curve being a Langmuir-like fit (see SI eq S1). Error bars are standard deviations. (b) Blinking statistics of individual defect sites in the diffusion-limited regime, where association rate is linearly dependent on the probe concentration, $k_1 = k_aC$. The linear fit gives an association rate constant k_a of 2.86 × 10^6 M^{-1} s^{-1} at a salt concentration of 400 mM KCl. The blinking ON time is independent of the probe concentration. (c) DFT calculation shows that 1-hexanethiol weakly attaches to one Mo atom at a monosulfur vacancy (V_S) forming V_S-thiol intermediate, whereas covalent bonding forms to three Mo atoms as the thiol becomes deprotonated forming V_S-thiolate. The presence of hydroxide ions stablizes the V_S-thiolate structure. A simplified reaction schematic illustrates the reversible and irreversible process. k_1 and k_2 are, respectively, the association and dissociation rate of a thiol probe and k_3 is the bleaching rate of a fluorophore. (d) Localization densities on MoS_2 flakes (colored squares) and substrates (gray squares) as a function of time in different pH. The densities are averaged over 5000 frames. Error bars are standard deviations. Data obtained at pH 7.7 and pH 8.8 are fitted with single exponential functions to estimate the decay rate (dashed lines). The probe used in all experiments is ATTO-dsDNA70bp-SH 10 nM in KCl 400 mM Tris 40 mM buffer with pH adjusted by adding HCl or KOH. The excitation power is 19 W/cm^2.

FRET effect is about 40 nm (inset in Figure 4f), matching with the range of dsDNA lengths used in our experiments.

As shown in Figure 4g, the intensity of detected binding events varies indeed according to the crystal structure of MoS_2 monolayer. Grain boundaries and line defects in MoS_2 have been reported as arrays of dislocations formed by atomic-ring structures at the intersection of two single-crystalline structures with different orientations.[12,41,48] The significantly reduced FRET rate on such defects could originate from disruption of the periodicity of the crystalline structure that changes the local dipoles of the MoS_2 crystal, thus hindering the electromagnetic wave coupling between the fluorophore and the MoS_2. In addition, strain around the boundaries can modify local band structures, thus affecting the absorption efficiency of certain energy.[49,50] However, further investigation is required to validate this hypothesis which is beyond the scope of this work.

Binding Kinetics and Defect Density. An important remaining question is the nature of the physicochemical interactions (reversible or irreversible binding) between the thiol probe and surface defects. We thus first investigated the adsorption of thiol probes on MoS_2 with probe concentrations ranging from 100 pM to 100 nM at pH 7.7. As reported in Figure 5a, we observe an increase in the density of localizations when increasing the thiol concentration, further reaching saturation for $c > 20$ nM, reminiscent of a Langmuir adsorption isotherm (implying indeed a reversible process over the time of this experiment, here each condition was measured within 15 min). Fitting the experimental data, we extract the dissociation constant, K_D as 6.5 ± 0.5 × 10^{-9} M at a salt concentration of 400 mM and pH 7.7 (see derivation of the fitting equation eq S1 in SI Section 5). The associated molar Gibbs free energy change can then be evaluated as ∼−47 kJ·mol^{-1} (19.3 k_BT) at room temperature (SI Section 6), consistent with predominantly weak physisorption over this short period of time. The schematic of this reversible binding is depicted in Figure 5c (orange).

By further analyzing the blinking statistics of each localization spot, the binding kinetic rates can be directly extracted. We get the association rate (k_1) and the association rate constant k_a from the reciprocal of the mean OFF time (or the interevent time) via $1/\tau_{OFF} = k_1 = k_aC$ in the diffusion-limited regime and the sum of the bleaching rate (k_3) of the fluorophore and the dissociation rate (k_2) of the thiol from the reciprocal of the mean ON time (event duration time) via $1/\tau_{ON} = k_3 + k_2$. Details on the extraction of blinking statistics are described in SI Section 8. As shown in Figure 5b, $1/\tau_{OFF}$ scales indeed linearly with the probe concentration, giving the association rate k_a = 2.86 × 10^6 M^{-1} s^{-1} for FAM-dsDNA70bp-SH at a salt concentration of 400 mM KCl. On the other hand,

https://doi.org/10.1021/acsnano.1c00373
ACS Nano 2021, 15, 7168−7178

the ON time does not depend on the probe concentration significantly and is limited by the bleaching of the fluorophore, giving the bleaching rate $k_3 \sim 3\ s^{-1}$ under excitation power density of 5 W/cm^2 (Figure S7). From $k_2 = K_D k_a$, we can extract $k_2 \sim 2 \times 10^{-2}\ s^{-1}$, implying that the thiol probe stays at a defect site for ~50 s on average.

Having quantified these kinetics, we can now estimate the density of the detectable sulfur vacancies in our experiments. Because of the fluorophore bleaching, the fraction of the fluorescently detectable defects is $\frac{k_2}{k_2 + k_3}$ according to eq S1. This is only about 0.7% under the experimental condition in Figure 5a. Given that the detectable binding saturation density in Figure 5a is 0.04 μm^{-2}, we estimate the density of the active sulfur vacancies interacting simultaneously with thiol probes in each frame in the aqueous solution of the order of 10 μm^{-2}. Using balanced super-resolution optical fluctuation imaging (bSOFI) to analyze the defect density as a function of imaging frames,[51] we observe that the density evaluation reaches stable estimation at 16 000 frames, that is, ~8 min (Figure S9). This implies that by this time all chemically active defects have been visited by the probes. Therefore, we extract the total chemically active defect density at the stable stage as ~2000 μm^{-2}. This is only 2% of the defect density 10^5 μm^{-2} as previously reported by TEM and STM investigation.[14,52] We speculate that this discrepancy may originate from the deactivation of sulfur vacancies by multiple sources, including ~20% polymer contamination coverage of MoS_2 from the transfer process (Figure S10), surface trapped air bubbles (Figure S11), different charge states of sulfur vacancy,[53] defect passivation by proton or oxygen.[54,55] Further investigation of the liquid/2D material interface by correlative AFM/2D-PAINT imaging may shed some light.[56,57] Nevertheless, the relative sulfur vacancy density mapped by our method can reveal the defect density variation over an area of 1000 μm^2 on the same sample (Figure 3 and Figure S4), as well as the comparison between different batches of samples (not shown here).

pH-Assisted Transition from Reversible to Irreversible Binding. Since all experiments in this work are carried out in an aqueous solution, one could expect the binding processes to be strongly affected by the environmental conditions and in particular by the pH of the solution. We thus investigated the interaction of thiol probes on MoS_2 over time and in different pH. As shown in Figure 5d, in an acidic pH environment (pH 3.6 and pH 5.4) the localization density of thiol probes binding to the defects shows a small initial increase, in which it remains constant over 4 h of measurements, pointing to a reversible interaction between thiol probes and sulfur vacancies. Conversely, at slightly basic conditions (pH 7.7 and pH 8.8) the localization density shows a clear decay over time, implying an irreversible binding process associated with the saturation of the reactive sulfur vacancies by thiol probes.

This transition from reversible to irreversible binding with increasing pH suggests a hydroxide-assisted transition from weak adsorption to strong binding. In particular, this transition occurs as the pH approaches the pK_a of the thiol probe (estimated as pH 10−12),[58] suggesting that thiol deprotonation could be responsible for the observed binding transition. A similar pH-dependent binding mechanism has been reported on the thiol-gold system.[59] To probe this hypothesis on MoS_2 in more detail, we resort to first-principle calculations based on the density functional theory (DFT) and *ab initio* molecular dynamics (AIMD) using 1-hexanethiol, which is the functional group of the imaging probe. Details of the calculations can be found in SI Section 11. The DFT results suggest that a thiol in its protonated form (−SH) will only weakly attach to one Mo atom at V_S forming a less stable V_S-thiol intermediate (Figure 5c). However, once weakly adsorbed, the V_S-thiol is likely to have a lower pK_a value than its counterpart in free solution, as the attached Mo at V_S is electron withdrawing. AIMD simulation indeed shows the V_S-thiol tends to get deprotonated with a small energy barrier of 0.17 eV and transitions into more stable form of V_S-thiolate (Figure 5c). The desorption energy barrier of the thiol from V_S is calculated as 1.484 eV for the lost proton that adsorbs on a nearby sulfur (MoS_2−H_{ads}) to reattach with the thiolate. The laser excitation in our experiments (2.54 eV) is plausibly the energy source for the desorption of thiol in a reversible process. However, the proton in MoS_2−H_{ads} can be subsequently taken away by hydroxide (OH^-) to form H_2O, leaving V_S-thiolate as the final product. Therefore, as the concentration of OH^- increases, irreversible binding is promoted by stabilized deprotonation of the thiol as it is temporally bound to the defect and through the increasing number of direct binding from the deprotonated thiol in free solution. Because of the high pK_a value of hexanethiol, we expect the direct binding of the deprotonated thiol to be rare, and deprotonation of the surface-bound thiol is more likely to be responsible for the irreversible binding. As can be seen in Figure 5d, the defect saturation with thiol probes is a rather slow process. By fitting the experimental data, we estimate the characteristic decay time to be 160 min at pH 7.7 and 70 min at pH 8.8. Although at pH 8.8 the decay is faster, we observe lower binding densities than at pH 7.7. This can be plausibly explained by a lower number of chemically active sites due to defect passivation by hydroxide shown by our DFT calculation and the increase of the negative surface charge of MoS_2 at higher pH.[19,60]

Note that in contrast to the previously reported V_S "healing" process in the gas phase,[26,28,61] we do not observe in our simulations spontaneous sulfur−carbon bond breakage in aqueous conditions, which is consistent with our experimental observations.

CONCLUSIONS

Combining PAINT methodology with defect-specific fluorescent probes allowed us to visualize nonradiative defects in 2D materials with resolution beyond the diffraction limit and with a high-throughput in aqueous conditions. This wide-field rapid mapping technique gives a global picture of the distribution of sulfur-deficient point-defects as well as grain boundaries and line defects across entire flakes of MoS_2 and WS_2. The 2D-PAINT fills the gap between the electron scanning microscopy and diffraction-limited far-field optical methods, with clear advantages of simplicity, fast-detection and compatibility in a liquid environment. By giving detailed insight on the interaction between functional groups and target defects, through analysis of single-molecule blinking statistics, this method could serve as a platform to study surface chemistry on 2D materials. Moreover, our demonstration of the distance-dependent FRET with the defect-anchored probes on MoS_2 on a single-molecule level is a promising step toward developing 2D-PAINT as a three-dimensional super-resolution methodology using a similar principle of metal-induced energy transfer, which has been recently demonstrated on graphene.[62] Finally, our method could be applied to other types of

https://doi.org/10.1021/acsnano.1c00373
ACS Nano 2021, 15, 7168−7178

nonradiative defects by versatile chemical modification of the fluorescent probes such as WSe_2. By bridging the gap between super-resolution microscopy and 2D materials, our work is thus an important step toward the multidimensional characterization tool that will facilitate defects engineering in 2D materials and propel the development of a variety of solid/liquid interfacial studies with 2D materials.

MATERIAL AND METHODS

MOCVD Growth. Monolayer MoS_2 is grown on *C*-plane sapphire substrates in a home-built system using the metal−organic chemical vapor deposition (MOCVD) method. As previously described, the sapphire substrate is annealed at 1000 °C (for 2 h in air) to achieve an atomically smooth surface for epitaxial growth.[63] Before growth, NaCl solution is spin-coated on the substrate to suppress nucleation and promote the growth.[64,65] The two precursors $Mo(CO)_6$ and H_2S, with the flow rate ratio of 1:6028 are carried by Ar gas to the MOCVD chamber and undergo reaction at 820 °C for 30 min. $Mo(CO)_6$ is kept at 15 °C in a water bath, and the valve is closed immediately after the growth process, whereas H_2S continues flowing during the cooling process. Throughout the whole growth process, the furnace is kept at 850 mbar pressure.

WS_2 is grown in the similar way via MOCVD method. The two precursors are $W(CO)_6$ and H_2S with the flow rate ratio of 1:2100. $W(CO)_6$ is kept at 25 °C in a water bath. The growth is carried out at 900 °C for 30 min under 850 mbar pressure.

Fluorescent Thiol Probes. Single stranded (ss) DNA with 5′ modification of thiol C6 and 3′ modification of ATTO-488 or FAM dyes were annealed in-house with complementary strands to form dsDNA probes: ATTO-dsDNA-SH and FAM-dsDNA-SH. ssDNA with 3′ modification of FAM were annealed with complementary strands to form dsDNA probes: FAM-dsDNA. Three lengths of DNA were used, namely 30bp, 50bp, and 70bp. All ssDNA products are ordered from MicroSynth. ATTO-SH were ordered from ATTO-TEC.

Microscope Setup. Imaging was carried out on a custom-built microscope that was described previously.[22] A schematic of the optical setup is depicted in Figure S1. Briefly, a coverslip with transferred 2D-TMDs is placed on an inverted microscope (IX71, Olympus) with a piezo stage (Nano-Drive, Mad City Labs Inc) driven with a feedback loop to minimize the drift in *z*-direction. A 100 mW 488 nm laser (Sapphire, Coherent) is used to excite the sample at an angle beyond the critical angle of the glass/water boundary (58.9°). The excitation power is controlled by an acousto-optic tunable filter (AOTFnC-VIS-TN, AA Opto-Electronic). The laser beam is focused at the back focal plane of the objective lens (UApo N ×100, NA 1.49, Olympus) to enable a wide-field illumination. The power density of the laser stated in the manuscript was measured after an objective lens with a normal incidence angle. The emission from the sample is collected by the same objective lens through a dichroic mirror (ZT488/561rpc, Chroma) and an emission filter (StopLine 405/488/568, Semrock). The emission goes further through precalibrated adaptive optics (micAO 3DSR, Imagine Optics) to minimize distortion of the point spread function. The emission of MoS_2 and fluorophores are split into two paths with wavelength windows of 509-530 nm and 675-725 nm by a dual-channel view optical system (DV2, Photometrics) with a dichroic mirror (T565lpxr, Chroma) and two emission filters (ET 525/36, ET 700/50, Chroma). The split images are projected adjacently to an EMCCD camera (iXon DU-897, Andor) with a back-projected pixel size of 105 nm.

Imaging Process. For each experiment, 5000 to 20000 frames of the dual-channel image were typically recorded. The gain of the EMCCD was set at 150 and the exposure time was set as 50 ms for a laser power density of 5 W/cm^2 and 30 ms for a higher excitation power. Between binding experiments with different fluorescent probes on the same MoS_2 samples, extensive washing by the buffer solution was performed to ensure a clean MoS_2 surface.

Localization Procedure. Centroids of the defect-bound fluorophores are localized using the FIJI plugin ThunderStrom.[66] Briefly, we first select the image area corresponding to fluorophore emission and apply a wavelet filter (B-Spline). Fluorophores with intensity peak higher than 1.5 × STD of the first wavelet level are selected for localization. The selected peaks are then fitted by 2D-Gaussian function to extract centroids. Lateral drift correction is done by cross-correlation of the reconstructed images.

Focused-Ion Beam Patterning. FIB irradiation and patterning were performed at Helios G4 PFIB UXe microscope using a focused xenon plasma beam. All investigated patterned samples were irradiated at a constant 90 μs dwell time, 2 μm pixel distance, and 30 kV beam with varying beam currents (10−100 pA) for different irradiation doses. The irradiation dose was calculated with the ion beam exposure formula for 2D materials.[67]

Raman Scattering Spectroscopy. Raman spectra of the monolayer MoS_2 flakes were collected by a (Renishaw inVia Confocal Raman Microscope) spectrometer at room temperature using a 532 nm laser with an excitation power of ∼1 mW. Point measurements were performed on the transferred MoS_2 flakes on glass substrates with or without prepatterned FIB irradiation. The excitation spot size is about 1 μm.

ASSOCIATED CONTENT

Supporting Information

The Supporting Information is available free of charge at https://pubs.acs.org/doi/10.1021/acsnano.1c00373.

Schematics of 2D-PAINT setup; AFM and Raman spectrum characterization of FIB patterned MoS_2; correlation between PL and localization density of WS_2; FRET quenching with ATTO-SH dye; analytical description and simulation of reversible binding process; photophysics of FAM and ATTO488 dyes; extraction of blinking statistics; bSOFI analysis; TEM and AFM characterization of MoS_2 surface; DFT and AIMD calculation; spatial autocorrelation analysis (PDF)

AUTHOR INFORMATION

Corresponding Authors

Miao Zhang − *Laboratory of Nanoscale Biology, Institute of Bioengineering, School of Engineering, École Polytechnique Fédérale de Lausanne (EPFL), 1015 Lausanne, Switzerland; Department of Applied Physics, KTH Royal Institute of Technology, 106 91 Stockholm, Sweden*; Email: miao.zhang@epfl.ch, miaoz@kth.se

Aleksandra Radenovic − *Laboratory of Nanoscale Biology, Institute of Bioengineering, School of Engineering, École Polytechnique Fédérale de Lausanne (EPFL), 1015 Lausanne, Switzerland*; orcid.org/0000-0001-8194-2785; Email: aleksandra.radenovic@epfl.ch

Authors

Martina Lihter − *Laboratory of Nanoscale Biology, Institute of Bioengineering, School of Engineering, École Polytechnique Fédérale de Lausanne (EPFL), 1015 Lausanne, Switzerland*; orcid.org/0000-0003-1859-8453

Tzu-Heng Chen − *Laboratory of Nanoscale Biology, Institute of Bioengineering, School of Engineering, École Polytechnique Fédérale de Lausanne (EPFL), 1015 Lausanne, Switzerland*

Michal Macha − *Laboratory of Nanoscale Biology, Institute of Bioengineering, School of Engineering, École Polytechnique Fédérale de Lausanne (EPFL), 1015 Lausanne, Switzerland*

Archith Rayabharam − *Department of Mechanical Science and Engineering, University of Illinois at Urbana−Champaign, Urbana 61801, Illinois, United States*

https://doi.org/10.1021/acsnano.1c00373
ACS Nano 2021, 15, 7168−7178

Karla Banjac − *Max Planck-EPFL Laboratory for Molecular Nanoscience and Institut de Physique, École Polytechnique Fédérale de Lausanne (EPFL), 1015 Lausanne, Switzerland;* orcid.org/0000-0001-7063-6213
Yanfei Zhao − *Electrical Engineering Institute and Institute of Materials Science and Engineering, École Polytechnique Fédérale de Lausanne (EPFL), 1015 Lausanne, Switzerland*
Zhenyu Wang − *Electrical Engineering Institute and Institute of Materials Science and Engineering, École Polytechnique Fédérale de Lausanne (EPFL), 1015 Lausanne, Switzerland*
Jing Zhang − *Electrical Engineering Institute and Institute of Materials Science and Engineering, École Polytechnique Fédérale de Lausanne (EPFL), 1015 Lausanne, Switzerland*
Jean Comtet − *Laboratory of Nanoscale Biology, Institute of Bioengineering, School of Engineering, École Polytechnique Fédérale de Lausanne (EPFL), 1015 Lausanne, Switzerland*
Narayana R. Aluru − *Department of Mechanical Science and Engineering, University of Illinois at Urbana−Champaign, Urbana 61801, Illinois, United States;* orcid.org/0000-0002-9622-7837
Magalí Lingenfelder − *Max Planck-EPFL Laboratory for Molecular Nanoscience and Institut de Physique, École Polytechnique Fédérale de Lausanne (EPFL), 1015 Lausanne, Switzerland;* orcid.org/0000-0003-1362-8879
Andras Kis − *Electrical Engineering Institute and Institute of Materials Science and Engineering, École Polytechnique Fédérale de Lausanne (EPFL), 1015 Lausanne, Switzerland;* orcid.org/0000-0002-3426-7702

Complete contact information is available at: https://pubs.acs.org/10.1021/acsnano.1c00373

Author Contributions

A. Radenovic conceived, supervised and coordinated all aspects of the projects. M.Z. and A. Radenovic designed the experiments. M.Z. performed the 2D-PAINT measurements and data analysis. M. Lihter designed the chemical agent and performed TEM imaging. T.C. performed the DFT calculation using Material Studio. A. Rayabharam performed DFT and AIMD simulation under supervision of N.R.A. M.M. performed FIB. K.B. performed AFM measurements. K.B. and M. Lingenfelder analyzed the AFM data. Y.Z. did the growth of MoS_2 and J.Z. did the growth of WS_2 under the supervision of A.K. Z.W. performed Raman spectroscopy measurements. M.Z. wrote the manuscript with input from A. Rayabharam, J.C., A. Radenovic, K.B., M. Lihter, and M. Lingenfelder.

Notes

The authors declare no competing financial interest.

ACKNOWLEDGMENTS

We acknowledge Prof. Ilya Sychukov for valuable discussions on the analytical analysis of binding kinetics. We acknowledge the support of Lely Feletti on DNA synthesis and the help of Adrien Descloux, Kristin Grussmayer, and Vytautas Navikas on fluorescence microscopy. M.Z. is grateful to Michael Graf for making the 3D schematics. This work was financially supported by the Swiss National Science Foundation (SNSF) Consolidator Grant (BIONIC BSCGI0_157802) and CCMX project ("Large Area Growth of 2D Materials for device integration"). M.Z. acknowledges support from the Swedish Research Council through the International Postdoc Grant (VR 2018-06764). A. Rayabharam and N.A. would like to acknowledge the Center for Enhanced Nanofluidic Transport (CENT), an Energy Frontier Research Center funded by the U.S. Department of Energy, Office of Science, Basic Energy Sciences under Award No. DE-SC0019112. A. Rayabharam and N.A. also acknowledge the Texas Advanced Computing Center (TACC) at The University of Texas at Austin for providing the computing resources on Stampede2 under the allocation TG-CDA100010.

REFERENCES

(1) Li, H.; Huang, J. K.; Shi, Y.; Li, L. J. Toward the Growth of High Mobility 2D Transition Metal Dichalcogenide Semiconductors. *Adv. Mater. Interfaces* **2019**, *6* (24), 1−21.
(2) Hu, Z.; Wu, Z.; Han, C.; He, J.; Ni, Z.; Chen, W. Two-Dimensional Transition Metal Dichalcogenides: Interface and Defect Engineering. *Chem. Soc. Rev.* **2018**, *47* (9), 3100−3128.
(3) He, Y. M.; Clark, G.; Schaibley, J. R.; He, Y.; Chen, M. C.; Wei, Y. J.; Ding, X.; Zhang, Q.; Yao, W.; Xu, X.; Lu, C. Y.; Pan, J. W. Single Quantum Emitters in Monolayer Semiconductors. *Nat. Nanotechnol.* **2015**, *10* (6), 497−502.
(4) Tran, T. T.; Bray, K.; Ford, M. J.; Toth, M.; Aharonovich, I. Quantum Emission from Hexagonal Boron Nitride Monolayers. *Nat. Nanotechnol.* **2016**, *11* (1), 37−41.
(5) Avsar, A.; Ciarrocchi, A.; Pizzochero, M.; Unuchek, D.; Yazyev, O. V.; Kis, A. Defect Induced, Layer-Modulated Magnetism in Ultrathin Metallic $PtSe_2$. *Nat. Nanotechnol.* **2019**, *14* (7), 674−678.
(6) Sangwan, V. K.; Jariwala, D.; Kim, I. S.; Chen, K. S.; Marks, T. J.; Lauhon, L. J.; Hersam, M. C. Gate-Tunable Memristive Phenomena Mediated by Grain Boundaries in Single-Layer MoS_2. *Nat. Nanotechnol.* **2015**, *10* (5), 403−406.
(7) Sangwan, V. K.; Lee, H. S.; Bergeron, H.; Balla, I.; Beck, M. E.; Chen, K. S.; Hersam, M. C. Multi-Terminal Memtransistors from Polycrystalline Monolayer Molybdenum Disulfide. *Nature* **2018**, *554* (7693), 500−504.
(8) Ye, G.; Gong, Y.; Lin, J.; Li, B.; He, Y.; Pantelides, S. T.; Zhou, W.; Vajtai, R.; Ajayan, P. M. Defects Engineered Monolayer MoS_2 for Improved Hydrogen Evolution Reaction. *Nano Lett.* **2016**, *16* (2), 1097−1103.
(9) Mitterreiter, E.; Liang, Y.; Golibrzuch, M.; McLaughlin, D.; Csoklich, C.; Bartl, J. D.; Holleitner, A.; Wurstbauer, U.; Bandarenka, A. S. *In-Situ* Visualization of Hydrogen Evolution Sites on Helium Ion Treated Molybdenum Dichalcogenides under Reaction Conditions. *npj 2D Mater. Appl.* **2019**, *3* (1), 1−9.
(10) Comtet, J.; Grosjean, B.; Glushkov, E.; Avsar, A.; Watanabe, K.; Taniguchi, T.; Vuilleumier, R.; Bocquet, M. L.; Radenovic, A. Direct Observation of Water-Mediated Single-Proton Transport between HBN Surface Defects. *Nat. Nanotechnol.* **2020**, *15* (7), 598−604.
(11) Hong, J.; Hu, Z.; Probert, M.; Li, K.; Lv, D.; Yang, X.; Gu, L.; Mao, N.; Feng, Q.; Xie, L.; Zhang, J.; Wu, D.; Zhang, Z.; Jin, C.; Ji, W.; Zhang, X.; Yuan, J.; Zhang, Z. Exploring Atomic Defects in Molybdenum Disulphide Monolayers. *Nat. Commun.* **2015**, *6*, 1−8.
(12) Zhou, W.; Zou, X.; Najmaei, S.; Liu, Z.; Shi, Y.; Kong, J.; Lou, J.; Ajayan, P. M.; Yakobson, B. I.; Idrobo, J. C. Intrinsic Structural Defects in Monolayer Molybdenum Disulfide. *Nano Lett.* **2013**, *13* (6), 2615−2622.
(13) Addou, R.; Colombo, L.; Wallace, R. M. Surface Defects on Natural MoS_2. *ACS Appl. Mater. Interfaces* **2015**, *7* (22), 11921−11929.
(14) Vancsó, P.; Magda, G. Z.; Peto, J.; Noh, J. Y.; Kim, Y. S.; Hwang, C.; Biró, L. P.; Tapasztó, L. The Intrinsic Defect Structure of Exfoliated MoS_2 Single Layers Revealed by Scanning Tunneling Microscopy. *Sci. Rep.* **2016**, *6* (April), 1−7.
(15) Parkin, W. M.; Balan, A.; Liang, L.; Das, P. M.; Lamparski, M.; Naylor, C. H.; Rodríguez-Manzo, J. A.; Johnson, A. T. C.; Meunier, V.; Drndić, M. Raman Shifts in Electron-Irradiated Monolayer MoS_2. *ACS Nano* **2016**, *10* (4), 4134−4142.
(16) Carozo, V.; Wang, Y.; Fujisawa, K.; Carvalho, B. R.; McCreary, A.; Feng, S.; Lin, Z.; Zhou, C.; Perea-López, N.; Elías, A. L.; Kabius,

B.; Crespi, V. H.; Terrones, M. Optical Identification of Sulfur Vacancies: Bound Excitons at the Edges of Monolayer Tungsten Disulfide. *Sci. Adv.* **2017**, *3* (4), e1602813.
(17) Bocquet, L.; Charlaix, E. Nanofluidics, from Bulk to Interfaces. *Chem. Soc. Rev.* **2010**, *39* (3), 1073−1095.
(18) Joly, L.; Tocci, G.; Merabia, S.; Michaelides, A. Strong Coupling between Nanofluidic Transport and Interfacial Chemistry: How Defect Reactivity Controls Liquid-Solid Friction through Hydrogen Bonding. *J. Phys. Chem. Lett.* **2016**, *7* (7), 1381−1386.
(19) Feng, J.; Graf, M.; Liu, K.; Ovchinnikov, D.; Dumcenco, D.; Heiranian, M.; Nandigana, V.; Aluru, N. R.; Kis, A.; Radenovic, A. Single-Layer MoS2 Nanopores as Nanopower Generators. *Nature* **2016**, *536* (7615), 197−200.
(20) Graf, M.; Lihter, M.; Unuchek, D.; Sarathy, A.; Leburton, J. P.; Kis, A.; Radenovic, A. Light-Enhanced Blue Energy Generation Using MoS2 Nanopores. *Joule* **2019**, *3* (6), 1549−1564.
(21) Li, H.; Tsai, C.; Koh, A. L.; Cai, L.; Contryman, A. W.; Fragapane, A. H.; Zhao, J.; Han, H. S.; Manoharan, H. C.; Abild-Pedersen, F.; Nørskov, J. K.; Zheng, X. Erratum: Activating and Optimizing MoS2 Basal Planes for Hydrogen Evolution through the Formation of Strained Sulphur Vacancies (Nature Materials (2016) 15 (48−53)). *Nat. Mater.* **2016**, *15* (3), 364.
(22) Feng, J.; Deschout, H.; Caneva, S.; Hofmann, S.; Lončarić, I.; Lazić, P.; Radenovic, A. Imaging of Optically Active Defects with Nanometer Resolution. *Nano Lett.* **2018**, *18* (3), 1739−1744.
(23) Comtet, J.; Glushkov, E.; Navikas, V.; Feng, J.; Babenko, V.; Hofmann, S.; Watanabe, K.; Taniguchi, T.; Radenovic, A. Wide-Field Spectral Super-Resolution Mapping of Optically Active Defects in Hexagonal Boron Nitride. *Nano Lett.* **2019**, *19*, 2516−2523.
(24) Thompson, R. E.; Larson, D. R.; Webb, W. W. Precise Nanometer Localization Analysis for Individual Fluorescent Probes. *Biophys. J.* **2002**, *82* (May), 2775−2783.
(25) Verhagen, T.; Guerra, V. L. P.; Haider, G.; Kalbac, M.; Vejpravova, J. Towards the Evaluation of Defects in MoS_2 Using Cryogenic Photoluminescence Spectroscopy. *Nanoscale* **2020**, *12* (5), 3019−3028.
(26) Förster, A.; Gemming, S.; Seifert, G.; Tománek, D. Chemical and Electronic Repair Mechanism of Defects in MoS_2 Monolayers. *ACS Nano* **2017**, *11* (10), 9989−9996.
(27) Makarova, M.; Okawa, Y.; Aono, M. Selective Adsorption of Thiol Molecules at Sulfur Vacancies on MoS_2(0001), Followed by Vacancy Repair *via* S-C Dissociation. *J. Phys. Chem. C* **2012**, *116* (42), 22411−22416.
(28) Yu, Z.; Pan, Y.; Shen, Y.; Wang, Z.; Ong, Z.; Xu, T.; Xin, R.; Pan, L.; Wang, B.; Sun, L.; Wang, J.; Zhang, G.; Zhang, Y. W.; Shi, Y.; Wang, X. Towards Intrinsic Charge Transport in Monolayer Molybdenum Disulfide by Defect and Interface Engineering Zhihao. *Nat. Commun.* **2014**, *5*, 1−7.
(29) Ding, Q.; Czech, K. J.; Zhao, Y.; Zhai, J.; Hamers, R. J.; Wright, J. C.; Jin, S. Basal-Plane Ligand Functionalization on Semiconducting 2H-MoS_2 Monolayers. *ACS Appl. Mater. Interfaces* **2017**, *9* (14), 12734−12742.
(30) Chou, S. S.; De, M.; Kim, J.; Byun, S.; Dykstra, C.; Yu, J.; Huang, J.; Dravid, V. P. Ligand Conjugation of Chemically Exfoliated MoS_2. *J. Am. Chem. Soc.* **2013**, *135* (12), 4584−4587.
(31) Sharonov, A.; Hochstrasser, R. M. Wide-Field Subdiffraction Imaging by Accumulated Binding of Diffusing Probes. *Proc. Natl. Acad. Sci. U. S. A.* **2006**, *103* (50), 18911−18916.
(32) Schnitzbauer, J.; Strauss, M. T.; Schlichthaerle, T.; Schueder, F.; Jungmann, R. Super-Resolution Microscopy with DNA-PAINT. *Nat. Protoc.* **2017**, *12* (6), 1198−1228.
(33) Jungmann, R.; Steinhauer, C.; Scheible, M.; Kuzyk, A.; Tinnefeld, P.; Simmel, F. C. Single-Molecule Kinetics and Super-Resolution Microscopy by Fluorescence Imaging of Transient Binding on DNA Origami. *Nano Lett.* **2010**, *10* (11), 4756−4761.
(34) Schueder, F.; Stein, J.; Stehr, F.; Auer, A.; Sperl, B.; Strauss, M. T.; Schwille, P.; Jungmann, R. An Order of Magnitude Faster DNA-PAINT Imaging by Optimized Sequence Design and Buffer Conditions. *Nat. Methods* **2019**, *16* (11), 1101−1104.
(35) Pujals, S.; Feiner-Gracia, N.; Delcanale, P.; Voets, I.; Albertazzi, L. Super-Resolution Microscopy as a Powerful Tool to Study Complex Synthetic Materials. *Nat. Rev. Chem.* **2019**, *3* (2), 68−84.
(36) Raja, A.; Montoya-Castillo, A.; Zultak, J.; Zhang, X. X.; Ye, Z.; Roquelet, C.; Chenet, D. A.; Van Der Zande, A. M.; Huang, P.; Jockusch, S.; Hone, J.; Reichman, D. R.; Brus, L. E.; Heinz, T. F. Energy Transfer from Quantum Dots to Graphene and MoS_2: The Role of Absorption and Screening in Two-Dimensional Materials. *Nano Lett.* **2016**, *16* (4), 2328−2333.
(37) Zhu, C.; Zeng, Z.; Li, H.; Li, F.; Fan, C.; Zhang, H. Single-Layer MoS_2-Based Nanoprobes for Homogeneous Detection of Biomolecules. *J. Am. Chem. Soc.* **2013**, *135* (16), 5998−6001.
(38) Graf, M.; Lihter, M.; Thakur, M.; Georgiou, V.; Topolancik, J.; Ilic, B. R.; Liu, K.; Feng, J.; Astier, Y.; Radenovic, A. Fabrication and Practical Applications of Molybdenum Disulfide Nanopores. *Nat. Protoc.* **2019**, *14* (4), 1130−1168.
(39) Splendiani, A.; Sun, L.; Zhang, Y.; Li, T.; Kim, J.; Chim, C.; Galli, G.; Wang, F. Emerging Photoluminescence in Monolayer. *Nano Lett.* **2010**, *10*, 1271−1275.
(40) Amani, M.; Burke, R. A.; Ji, X.; Zhao, P.; Lien, D. H.; Taheri, P.; Ahn, G. H.; Kirya, D.; Ager, J. W.; Yablonovitch, E.; Kong, J.; Dubey, M.; Javey, A. High Luminescence Efficiency in MoS_2 Grown by Chemical Vapor Deposition. *ACS Nano* **2016**, *10* (7), 6535−6541.
(41) Van Der Zande, A. M.; Huang, P. Y.; Chenet, D. A.; Berkelbach, T. C.; You, Y.; Lee, G. H.; Heinz, T. F.; Reichman, D. R.; Muller, D. A.; Hone, J. C. Grains and Grain Boundaries in Highly Crystalline Monolayer Molybdenum Disulphide. *Nat. Mater.* **2013**, *12* (6), 554−561.
(42) Ghorbani-Asl, M.; Kretschmer, S.; Spearot, D. E.; Krasheninnikov, A. V. Two-Dimensional MoS_2 under Ion Irradiation: From Controlled Defect Production to Electronic Structure Engineering. *2D Mater.* **2017**, *4* (2), 025078.
(43) Mignuzzi, S.; Pollard, A. J.; Bonini, N.; Brennan, B.; Gilmore, I. S.; Pimenta, M. A.; Richards, D.; Roy, D. Effect of Disorder on Raman Scattering of Single-Layer MoS_2. *Phys. Rev. B: Condens. Matter Mater. Phys.* **2015**, *91* (19), 1−7.
(44) Kang, N.; Paudel, H. P.; Leuenberger, M. N.; Tetard, L.; Khondaker, S. I. Photoluminescence Quenching in Single-Layer MoS_2 *via* Oxygen Plasma Treatment. *J. Phys. Chem. C* **2014**, *118* (36), 21258−21263.
(45) Kastl, C.; Koch, R. J.; Chen, C. T.; Eichhorn, J.; Ulstrup, S.; Bostwick, A.; Jozwiak, C.; Kuykendall, T. R.; Borys, N. J.; Toma, F. M.; Aloni, S.; Weber-Bargioni, A.; Rotenberg, E.; Schwartzberg, A. M. Effects of Defects on Band Structure and Excitons in WS_2 Revealed by Nanoscale Photoemission Spectroscopy. *ACS Nano* **2019**, *13* (2), 1284−1291.
(46) Rosenberger, M. R.; Chuang, H. J.; McCreary, K. M.; Li, C. H.; Jonker, B. T. Electrical Characterization of Discrete Defects and Impact of Defect Density on Photoluminescence in Monolayer WS_2. *ACS Nano* **2018**, *12* (2), 1793−1800.
(47) Stellwagen, N. C.; Magnusdottir, S.; Gelfi, C.; Righetti, P. G. Measuring the Translational Diffusion Coefficients of Small DNA Molecules by Capillary Electrophoresis. *Biopolymers* **2001**, *58* (4), 390−397.
(48) Najmaei, S.; Liu, Z.; Zhou, W.; Zou, X.; Shi, G.; Lei, S.; Yakobson, B. I.; Idrobo, J. C.; Ajayan, P. M.; Lou, J. Vapour Phase Growth and Grain Boundary Structure of Molybdenum Disulphide Atomic Layers. *Nat. Mater.* **2013**, *12* (8), 754−759.
(49) Shi, H.; Pan, H.; Zhang, Y. W.; Yakobson, B. I. Quasiparticle Band Structures and Optical Properties of Strained Monolayer MoS_2 and WS_2. *Phys. Rev. B: Condens. Matter Mater. Phys.* **2013**, *87* (15), 1−8.
(50) Conley, H. J.; Wang, B.; Ziegler, J. I.; Haglund, R. F.; Pantelides, S. T.; Bolotin, K. I. Bandgap Engineering of Strained Monolayer and Bilayer MoS_2. *Nano Lett.* **2013**, *13* (8), 3626−3630.
(51) Geissbuehler, S.; Bocchio, N. L.; Dellagiacoma, C.; Berclaz, C.; Leutenegger, M.; Lasser, T. Mapping Molecular Statistics with Balanced Super-Resolution Optical Fluctuation Imaging (BSOFI). *Opt. Nanoscopy* **2012**, *1* (1), 4.

https://doi.org/10.1021/acsnano.1c00373
ACS Nano 2021, 15, 7168−7178

(52) Lin, J.; Pantelides, S. T.; Zhou, W. Vacancy-Induced Formation and Growth of Inversion Domains in Transition-Metal Dichalcogenide Monolayer. *ACS Nano* **2015**, *9* (5), 5189−5197.
(53) Song, S. H.; Joo, M. K.; Neumann, M.; Kim, H.; Lee, Y. H. Probing Defect Dynamics in Monolayer MoS_2 *via* Noise Nanospectroscopy. *Nat. Commun.* **2017**, *8* (1), 1−5.
(54) Kiriya, D.; Hijikata, Y.; Pirillo, J.; Kitaura, R.; Murai, A.; Ashida, A.; Yoshimura, T.; Fujimura, N. Systematic Study of Photoluminescence Enhancement in Monolayer Molybdenum Disulfide by Acid Treatment. *Langmuir* **2018**, *34* (35), 10243−10249.
(55) Lu, H.; Kummel, A.; Robertson, J. Passivating the Sulfur Vacancy in Monolayer MoS2. *APL Mater.* **2018**, *6*, 066104.
(56) Odermatt, P. D.; Shivanandan, A.; Deschout, H.; Jankele, R.; Nievergelt, A. P.; Feletti, L.; Davidson, M. W.; Radenovic, A.; Fantner, G. E. High-Resolution Correlative Microscopy: Bridging the Gap between Single Molecule Localization Microscopy and Atomic Force Microscopy. *Nano Lett.* **2015**, *15* (8), 4896−4904.
(57) Beuwer, M. A.; Knopper, M. F.; Albertazzi, L.; Van Der Zwaag, D.; Ellenbroek, W. G.; Meijer, E. W.; Prins, M. W. J.; Zijlstra, P. Mechanical Properties of Single Supramolecular Polymers from Correlative AFM and Fluorescence Microscopy. *Polym. Chem.* **2016**, *7* (47), 7260−7268.
(58) Zheng, Y.; Zheng, W.; Zhu, D.; Chang, H. Theoretical Modeling of PKa's of Thiol Compounds in Aqueous Solution. *New J. Chem.* **2019**, *43* (13), 5239−5254.
(59) Xue, Y.; Li, X.; Li, H.; Zhang, W. Quantifying Thiol-Gold Interactions towards the Efficient Strength Control. *Nat. Commun.* **2014**, *5*, 4348.
(60) Ge, P.; Scanlon, M. D.; Peljo, P.; Bian, X.; Vubrel, H.; O'Neill, A.; Coleman, J. N.; Cantoni, M.; Hu, X.; Kontturi, K.; Liu, B. H.; Girault, H. H. Hydrogen Evolution across Nano-Schottky Junctions at Carbon Supported MoS_2 Catalysts in Biphasic Liquid Systems. *Chem. Commun.* **2012**, *48* (52), 6484−6486.
(61) Li, Q.; Zhao, Y.; Ling, C.; Yuan, S.; Chen, Q.; Wang, J. Towards a Comprehensive Understanding of the Reaction Mechanisms between Defective MoS_2 and Thiol Molecules. *Angew. Chem., Int. Ed.* **2017**, *56* (35), 10501−10505.
(62) Ghosh, A.; Sharma, A.; Chizhik, A. I.; Isbaner, S.; Ruhlandt, D.; Tsukanov, R.; Gregor, I.; Karedla, N.; Enderlein, J. Graphene-Based Metal-Induced Energy Transfer for Sub-Nanometre Optical Localization. *Nat. Photonics* **2019**, *13*, 860−865.
(63) Dumcenco, D.; Ovchinnikov, D.; Marinov, K.; Lazić, P.; Gibertini, M.; Marzari, N.; Sanchez, O. L.; Kung, Y. C.; Krasnozhon, D.; Chen, M. W.; Bertolazzi, S.; Gillet, P.; Fontcuberta I Morral, A.; Radenovic, A.; Kis, A. Large-Area Epitaxial Monolayer MoS_2. *ACS Nano* **2015**, *9* (4), 4611−4620.
(64) Kim, H.; Ovchinnikov, D.; Deiana, D.; Unuchek, D.; Kis, A. Suppressing Nucleation in Metal-Organic Chemical Vapor Deposition of MoS_2 Monolayers by Alkali Metal Halides. *Nano Lett.* **2017**, *17* (8), 5056−5063.
(65) Cun, H.; Macha, M.; Kim, H. K.; Liu, K.; Zhao, Y.; LaGrange, T.; Kis, A.; Radenovic, A. Wafer-Scale MOCVD Growth of Monolayer MoS_2 on Sapphire and SiO_2. *Nano Res.* **2019**, *12* (10), 2646−2652.
(66) Ovesný, M.; Křížek, P.; Borkovec, J.; Švindrych, Z.; Hagen, G. M. ThunderSTORM: A Comprehensive ImageJ Plug-In for PALM and STORM Data Analysis and Super-Resolution Imaging. *Bioinformatics* **2014**, *30* (16), 2389−2390.
(67) Thiruraman, J. P.; Masih Das, P.; Drndić, M. Irradiation of Transition Metal Dichalcogenides Using a Focused Ion Beam: Controlled Single-Atom Defect Creation. *Adv. Funct. Mater.* **2019**, *29* (52), 1904668.

https://doi.org/10.1021/acsnano.1c00373
ACS Nano 2021, 15, 7168−7178